Modeling the viscoplastic response of supramolecular elastomers

Drozdov, A.D.; Christiansen, J. deClaville

Published in:
International Journal of Solids and Structures

DOI (link to publication from Publisher):
10.1016/j.ijsolstr.2022.111919

Publication date:
2022

Document Version
Publisher's PDF, also known as Version of record

International Journal of Solids and Structures 254–255 (2022) 111919

Contents lists available at ScienceDirect

International Journal of Solids and Structures

journal homepage: www.elsevier.com/locate/ijsolstr

Modeling the viscoplastic response of supramolecular elastomers

A.D. Drozdov *, J. deClaville Christiansen

Department of Materials and Production, Aalborg University, Fibigerstraede 16, Aalborg 9220, Denmark

ARTICLE INFO

Keywords:
Supramolecular elastomer
Viscoplasticity
Constitutive modeling
Structure–property relations

ABSTRACT

Mechanical properties of supramolecular elastomers (reversible polymer networks with chains connected by supramolecular and dynamic covalent bonds) differ noticeably from those of conventional elastomers with covalent cross-links. Due to the ability of supramolecular polymers to be reprocessed, reshaped, recycled and reused, they are considered as potential candidates for green and sustainable economy. A simple model is developed for the viscoplastic behavior of supramolecular elastomers at large strains. The model involves only four to five material parameters and describes adequately the response of supramolecular elastomers under tension, compression and cyclic loading in a unified manner. The governing equations are applied to the analysis of experimental stress–strain diagrams on supramolecular elastomers with various types of reversible bonds. Good agreement is revealed between the observations and results of numerical analysis. Correlations are established between types and concentrations of supramolecular bonds and adjustable parameters in the model.

1. Introduction

Good mechanical properties of vulcanized rubbers, their robustness, high thermal stability and exceptional chemical resistance are ensured by chemical cross-linking of polymer chains. However, networks of chains bridged by covalent bonds cannot be easily reprocessed, which makes these materials one of the major challenges for the circular economy. To reduce waste pollution, conventional elastomers (where chains form permanent networks) are replaced with sustainable compounds (whose chains are organized in reversible networks) that can be reshaped, recycled and reused (Wemyss et al., 2020). In these reversible networks, chains are bridged by intermolecular complexes (Aida et al., 2012) created via supramolecular interactions (metal–ligand coordination complexes, electrostatic interactions, double and quadruple hydrogen bonds, host-guest interactions, van der Waals forces, etc.) and/or dynamic covalent bonds (Samanta et al., 2021).

The presence of reversible bonds between chains not only ensure recyclability of supramolecular elastomers (Imbernon and Norvez, 2016; Luo et al., 2022) and extends their lifetime due to the self-healing ability of these materials (Wang and Urban, 2020), but opens novel areas for their potential applications (O'Donnell et al., 2022) as materials for biomimetic impact protective devices (Liu et al., 2021), stretchable electronics (Kang et al., 2019) and wearable implantable systems (Ray et al., 2019).

Replacement of covalent cross-links between chains with non-covalent reversible bonds results in an enhancement of mechanical properties of polymer networks. Unlike vulcanized rubbers whose strain at break ϵ_b under uniaxial tension remains below 10, supramolecular elastomers and hydrogels demonstrate extreme stretchability with ϵ_b exceeding 100 (Liu et al., 2017), engineering tensile stress at break σ_b above 70 MPa, and fracture energy exceeding 200 kJ/m^2 (Li et al., 2021b). The exceptionally high strength, stretchability and toughness are reached due to an optimal combination of reversible bonds with various strengths and rates of rearrangement (Yang et al., 2019; Huo et al., 2021; Rodin et al., 2021).

Design of supramolecular elastomers and development of new routes for their manufacturing require detailed characterization of their behavior under various regimes of loading, as well as simple and reliable constitutive models for the mechanical response, energy dissipation and fracture (Kajita et al., 2017; Chen et al., 2021).

Several models for the viscoelastoplastic response of supramolecular hydrogels and elastomers have been developed in the past decade (Long et al., 2014; Guo et al., 2016; Mao et al., 2017; Vernerey et al., 2017; Vernerey, 2018; Drozdov and deClaville Christiansen, 2018a,b,c; Yu et al., 2018; Zhou et al., 2018; Elziere et al., 2019; Morovati and Dargazany, 2019; Xiang et al., 2019; Drozdov and deClaville Christiansen, 2020a,b; Lin et al., 2020; Saadedine et al., 2021). Majority of these studies focused on the time-dependent behavior of polymer networks and description of self-healing, self-recovery and anti-fatigue phenomena. Less attention has been paid, however, to modeling the mechanical behavior of supramolecular elastomers at very

* Corresponding author.
E-mail address: aleksey@m-tech.aau.dk (A.D. Drozdov).

https://doi.org/10.1016/j.ijsolstr.2022.111919
Received 31 March 2022; Received in revised form 1 August 2022; Accepted 3 August 2022
Available online 8 August 2022

large deformations (up to breakage of specimens) and the influence of chemical structure of reversible bonds on the stress–strain diagrams under tension, compression and cyclic deformations.

The objective of this study is threefold: (i) to develop a simple model (with only four to five material constants) for the viscoplastic response of supramolecular elastomers under quasi-static loading with finite strains, (ii) to determine material parameters by fitting experimental data in uniaxial tensile, compressive and cyclic tests on elastomers with various types of reversible bonds, and (iii) to examine how these parameters are affected by the strain rate and concentration of supramolecular bonds.

To minimize the number of adjustable parameters in the governing equations, we consider isothermal deformation at room temperature (only the effect of strain rate is taken into account) and focus on the analysis of elastomers with metal–ligand coordination bonds, weak and strong H-bonds, dynamic covalent bonds, and their combinations. The latter is of particular importance for (i) understanding the synergy of interactions between various types of supramolecular bonds (Huo et al., 2021) and (ii) design of supramolecular polymers with tunable mechanical properties (Xu et al., 2018).

To make the model tractable, we confine ourselves to the analysis of supramolecular elastomers with weak viscoelasticity (for all elastomers under consideration, their loss tangent remains below 0.1). The mechanical behavior of these materials is entirely characterized by tensile tests with a limited interval of strain rates, while creep and relaxation tests are not used in the experimental analysis. The viscoelastic response of supramolecular polymers becomes important when chains in a polymer network are connected by rapid and slow temporary bonds that reveal the synergy of their interactions (Rosales and Anseth, 2016; Richardson et al., 2019; Rizwan et al., 2021; Drozdov and deClaville Christiansen, 2022). However, introduction of slow bonds appears to be unfavorable for development of supertough elastomeric materials (which are the subject of this study), as these bonds behave as permanent cross-links under rapid loading and reduce substantially the strain at break.

The novelty of this research consists in the following. A model with a small number of adjustable parameters is derived in finite viscoplasticity of supramolecular elastomers. The ability of the model to describe experimental stress–strain diagrams under tension and compression (up to breakage of samples) and cyclic deformations (with large maximum strains) is confirmed by comparison with observations on several supramolecular elastomers. An advantage of the proposed approach is that it allows the effect of various types of supramolecular bonds on the mechanical response to be assessed quantitatively. Simple analytical relations are introduced to characterize the influence of strain rate and concentration of metal–ligand bonds on material parameters.

Although the model is derived for an arbitrary three-dimensional deformation, its ability to describe experimental data is validated by comparison of results of numerical analysis with observations in uniaxial tensile–compressive tests only. This is caused by (i) the lack of experimental data on supramolecular elastomers under multiaxial loading and (ii) potential applications of these materials in the biomedical and energy fields, where they are subjected to uniaxial loading only: electrocardiography–electromyography sensors (Kang et al., 2019), wearable diabetes patches (Huo et al., 2021), microparticles for biological imaging (Yang et al., 2021), thin films for environmental detection, photovoltaic devices and triboelectrical generators (O'Donnell et al., 2022).

The exposition is organized as follows. A detailed derivation of the model is provided in Section 2. Fitting of experimental data is performed in Section 3. Distinctions between the responses of covalently cross-linked and supramolecular elastomers are discussed in Section 4. Concluding remarks are formulated in Section 5.

2. Constitutive model

A supramolecular elastomer is modeled as an isotropic and homogeneous viscoplastic medium. Its viscoelastic response is disregarded. To examine the model, experimental data on supramolecular elastomers are fitted in Section 3 in tensile and compressive tests with the strain rates belonging to the interval between 0.01 and 1 s^{-1}. Observations on these materials in small-amplitude oscillatory tests show that their loss tangent remains below 0.1 in the standard frequency window ranging from 0.01 to 100 s^{-1}.

The initial state of the elastomer coincides with that for an undeformed specimen. Transformation of the initial state into the actual state is described by the deformation gradient $\mathbf{F}$. Adopting the affine hypothesis, we suppose that deformation of the polymer network coincides with macro-deformation.

The viscoplastic deformation is treated as transition from the initial state to the reference (stress-free) state of the polymer network. The deformation gradient for viscoplastic deformation is denoted by $\mathbf{F}_p$. It follows from the multiplicative decomposition formula that

$$\mathbf{F} = \mathbf{F}_e \cdot \mathbf{F}_p, \tag{1}$$

where the dot stands for inner product, and $\mathbf{F}_e$ denotes the deformation gradient for elastic deformation.

The velocity gradient for macro-deformation reads

$$\mathbf{L} = \dot{\mathbf{F}} \cdot \mathbf{F}^{-1}, \tag{2}$$

where the superscript dot stands for the derivative with respect to time. It follows from Eqs. (1) and (2) that

$$\mathbf{L} = \mathbf{L}_e + \mathbf{L}_p, \tag{3}$$

where

$$\mathbf{L}_e = \dot{\mathbf{F}}_e \cdot \mathbf{F}_e^{-1}, \qquad \mathbf{L}_p = \mathbf{F}_e \cdot \mathbf{l}_p \cdot \mathbf{F}_e^{-1}, \qquad \mathbf{l}_p = \dot{\mathbf{F}}_p \cdot \mathbf{F}_p^{-1}. \tag{4}$$

Following the conventional approach, we disregard plastic spin and presume the velocity gradient $\mathbf{l}_p$ to be symmetric, $\mathbf{l}_p = \mathbf{d}_p$, where $\mathbf{d}_p = \frac{1}{2}(\mathbf{l}_p + \mathbf{l}_p^\top)$ is the rate-of-strain tensor for plastic deformation, and $\top$ stands for transpose. Eqs. (3) and (4) imply that

$$\mathbf{D} = \mathbf{D}_e + \mathbf{D}_p, \tag{5}$$

where

$$\mathbf{D} = \frac{1}{2}(\mathbf{L} + \mathbf{L}^\top), \qquad \mathbf{D}_e = \frac{1}{2}(\mathbf{L}_e + \mathbf{L}_e^\top), \qquad \mathbf{D}_p = \frac{1}{2}(\mathbf{L}_p + \mathbf{L}_p^\top) \tag{6}$$

with

$$\mathbf{D}_p = \frac{1}{2}\left(\mathbf{F}_e \cdot \mathbf{d}_p \cdot \mathbf{F}_e^{-1} + \mathbf{F}_e^{-\top} \cdot \mathbf{d}_p \cdot \mathbf{F}_e^{\top}\right). \tag{7}$$

With reference to (Drozdov et al., 2013), we suppose that the viscoplastic deformation is caused by two reasons: (i) the plastic flow of junctions between chains induced by macro-deformation (with the rate-of-strain tensor $\mathbf{d}_m$) and (ii) their plastic flow driven by inter-chain interaction (with the rate-of-strain tensor $\mathbf{d}_i$). The first mechanism describes slippage of entanglements between chains, while the other mechanism is typical of polymer networks with chains bridged by supramolecular bonds (Filippidi et al., 2017). The rate-of-strain tensor for the total plastic deformation reads

$$\mathbf{d}_p = \mathbf{d}_m + \mathbf{d}_i. \tag{8}$$

Insertion of expression (8) into Eqs. (5) and (7) yields

$$\mathbf{D} = \mathbf{D}_e + \mathbf{D}_m + \mathbf{D}_i \tag{9}$$

with

$$\mathbf{D}_m = \frac{1}{2}\left(\mathbf{F}_e \cdot \mathbf{d}_m \cdot \mathbf{F}_e^{-1} + \mathbf{F}_e^{-\top} \cdot \mathbf{d}_m \cdot \mathbf{F}_e^{\top}\right), \qquad \mathbf{D}_i = \frac{1}{2}\left(\mathbf{F}_e \cdot \mathbf{d}_i \cdot \mathbf{F}_e^{-1} + \mathbf{F}_e^{-\top} \cdot \mathbf{d}_i \cdot \mathbf{F}_e^{\top}\right). \tag{10}$$

The rate-of-strain tensor for sliding of junctions is presumed to be proportional to the rate-of-strain tensor for macro-deformation,

$$\mathbf{D}_{\rm m} = \phi \mathbf{D}. \tag{11}$$

The non-negative function ϕ in Eq. (11) obeys the conditions: (i) ϕ vanishes in the initial state (at infinitesimal strains, slippage of entanglements is negligible), (ii) ϕ increases with macro-deformation (the viscoplastic flow is accelerated under loading), and (iii) ϕ tends to its ultimate value $\phi = 1$ at very large strains. Eqs. (9) and (11) imply that

$$\mathbf{D}_{\rm e} = (1-\phi)\mathbf{D} - \mathbf{D}_{\rm i}. \tag{12}$$

The left and right Cauchy–Green tensors for elastic deformation are given by

$$\mathbf{B}_{\rm e} = \mathbf{F}_{\rm e} \cdot \mathbf{F}_{\rm e}^{\rm T}, \qquad \mathbf{C}_{\rm e} = \mathbf{F}_{\rm e}^{\rm T} \cdot \mathbf{F}_{\rm e}. \tag{13}$$

The incompressibility conditions for macro-deformation and plastic deformation read

$$\mathbf{I} : \mathbf{D} = 0, \qquad \mathbf{I} : \mathbf{d}_{\rm i} = 0, \tag{14}$$

where $\mathbf{I}$ is the unit tensor, and the colon stands for contraction. The first two principal invariants $I_{\rm e1}$, $I_{\rm e2}$ of the Cauchy–Green tensors for elastic deformation obey the equations

$$\dot I_{\rm e1} = 2\mathbf{B}_{\rm e} : \mathbf{D}_{\rm e}, \qquad \dot I_{\rm e2} = 2\Big(I_{\rm e2}\mathbf{I} - I_{\rm e3}\mathbf{B}_{\rm e}^{-1}\Big) : \mathbf{D}_{\rm e}, \tag{15}$$

whereas their third principal invariant $I_{\rm e3}$ equals unity. Inserting Eq. (12) into Eq. (15) and using Eqs. (7) and (14), we find that

$$\dot I_{\rm e1} = 2\Big[(1-\phi)\mathbf{B}_{\rm e} : \mathbf{D} - \mathbf{C}_{\rm e} : \mathbf{d}_{\rm i}\Big], \qquad \dot I_{\rm e2} = -2\Big[(1-\phi)\mathbf{B}_{\rm e}^{-1} : \mathbf{D} - \mathbf{C}_{\rm e}^{-1} : \mathbf{d}_{\rm i}\Big]. \tag{16}$$

The strain energy density W of a polymer network is treated as a function of the principal invariants $I_{\rm e1}$, $I_{\rm e2}$ of the Cauchy–Green tensor for elastic deformation. Constitutive equations for a supramolecular elastomer under isothermal deformation are developed by means of the free energy imbalance inequality

$$\dot W - u_{\rm mec} \le 0, \tag{17}$$

where $u_{\rm mec} = \boldsymbol{\Sigma} : \mathbf{D}$ denotes the work (per unit volume and unit time) produced by external loads, and $\boldsymbol{\Sigma}$ is the Cauchy stress tensor.

Eq. (17) is fulfilled when the deformation gradient $\mathbf{F}$ obeys the incompressibility condition (14). To account for this condition, we multiply the first equality in Eq. (14) by an arbitrary function Π (pressure treated as a Lagrange multiplier), add the result to Eq. (17), use Eqs. (16), and find that

$$[2\mathbf{K}_{\rm e} - (\boldsymbol{\Sigma} + \Pi\mathbf{I})] : \mathbf{D} - 2\mathbf{K}_{\rm i} : \mathbf{d}_{\rm i} \le 0 \tag{18}$$

with

$$\mathbf{K}_{\rm e} = (1-\phi)\Big(W_{,1}\mathbf{B}_{\rm e} - W_{,2}\mathbf{B}_{\rm e}^{-1}\Big), \qquad \mathbf{K}_{\rm i} = \Big(W_{,1}\mathbf{C}_{\rm e} - W_{,2}\mathbf{C}_{\rm e}^{-1}\Big)',$$

where $W_{,m} = \partial W/\partial I_{em}$ $(m = 1,2)$, and the prime stands for the deviatoric component of a tensor. Keeping in mind that $\mathbf{D}$ is an arbitrary function, while $\mathbf{d}_{\rm i}$ is an arbitrary function obeying Eq. (14), we conclude that Eq. (18) is satisfied, provided that the Cauchy stress tensor reads

$$\boldsymbol{\Sigma} = -\Pi\,\mathbf{I} + 2(1-\phi)\Big(W_{,1}\mathbf{B}_{\rm e} - W_{,2}\mathbf{B}_{\rm e}^{-1}\Big), \tag{19}$$

and the plastic flow induced by inter-chain interaction is governed by the equation

$$\mathbf{d}_{\rm i} = \mathcal{P}_0\Big[\Big(W_{,1}\mathbf{C}_{\rm e} - W_{,2}\mathbf{C}_{\rm e}^{-1}\Big) - \frac{1}{3}\Big(W_{,1}I_{\rm e1} - W_{,2}I_{\rm e2}\Big)\mathbf{I}\Big], \tag{20}$$

where $\mathcal{P}_0$ is an arbitrary non-negative function.

For definiteness, we accept the Gent formula (Gent, 1996) for the specific mechanical energy of the polymer network,

$$W = -\frac{1}{2}GK\ln\Big(1 - \frac{I_{\rm e1}-3}{K}\Big), \tag{21}$$

where G stands for the shear modulus, and K is a constant accounting for finite extensibility of chains. When $K = \infty$, Eq. (21) is transformed into the conventional neo-Hookean equation

$$W = \frac{1}{2}G(I_{\rm e1} - 3) \tag{22}$$

with the only material parameter G. Substitution of Eq. (21) into Eq. (19) implies that

$$\boldsymbol{\Sigma} = -\Pi\,\mathbf{I} + GV(1-\phi)\mathbf{B}_{\rm e} \tag{23}$$

with

$$V = \Big(1 - \frac{I_{\rm e1}-3}{K}\Big)^{-1}. \tag{24}$$

Insertion of Eq. (21) into Eq. (20) implies that

$$\mathbf{d}_{\rm i} = \frac{3}{2}\mathcal{P}V\Big(\mathbf{C}_{\rm e} - \frac{1}{3}I_{\rm e1}\mathbf{I}\Big), \tag{25}$$

where $\mathcal{P} = \mathcal{P}_0 G/3$.

Eqs. (23)–(25) provide constitutive equations for the viscoplastic response of supramolecular elastomers under arbitrary three-dimensional deformations with finite strains. These relations involve two coefficients, G and K, characterizing the strain energy density W, and two functions, ϕ and $\mathcal{P}$, governing the viscoplastic flow.

The following equation is adopted for the function ϕ:

$$\frac{{\rm d}\phi}{{\rm d}t} = \frac{aD_{\rm eq}}{I_{\rm e1}}(1-\phi)^2, \qquad \phi(0) = 0. \tag{26}$$

Here $t = 0$ stands for the instant when loads are applied, a is a non-negative coefficient, and

$$D_{\rm eq} = \sqrt{\frac{2}{3}\mathbf{D} : \mathbf{D}} \tag{27}$$

denotes the equivalent strain rate for macro-deformation. Eq. (26) ensures that all conditions imposed on the coefficient of proportionality in Eq. (11) are fulfilled. The physical meaning of Eq. (26) will be discussed in what follows.

The function $\mathcal{P}$ is introduced to describe cyclic deformations. We suppose that $\mathcal{P}$ vanishes under active loading and accept positive values under unloading,

$$\mathcal{P} = 0 \quad \text{(loading)}, \qquad \mathcal{P} > 0 \quad \text{(unloading)}. \tag{28}$$

Its behavior under retraction is governed by the equation

$$\mathcal{P} = P\exp(-\alpha\Sigma_{\rm eq}^*), \tag{29}$$

where P and α are material parameters, $\boldsymbol{\Sigma}^*$ is the Cauchy stress tensor at the instant when unloading starts, and

$$\Sigma_{\rm eq}^* = \sqrt{(\boldsymbol{\Sigma}^* - \boldsymbol{\Sigma}) : (\boldsymbol{\Sigma}^* - \boldsymbol{\Sigma})} \tag{30}$$

is the equivalent difference between $\boldsymbol{\Sigma}^*$ and the current stress $\boldsymbol{\Sigma}$. Eq. (29) means that the rate of viscoplastic flow caused by inter-chains interactions reaches its maximum at the instant when unloading starts and decays exponentially when the stress reduces under retraction.

Under uniaxial tension, the deformation gradient for macro-deformation reads

$$\mathbf{F} = \lambda \boldsymbol{i}_1\boldsymbol{i}_1 + \frac{1}{\sqrt{\lambda}}(\boldsymbol{i}_2\boldsymbol{i}_2 + \boldsymbol{i}_3\boldsymbol{i}_3), \tag{31}$$

where λ stands for elongation ratio, and $\boldsymbol{i}_m$ $(m = 1,2,3)$ are unit vectors of a Cartesian frame. It follows from Eqs. (2), (6) and (31) that

$$\mathbf{D} = \frac{\dot\lambda}{\lambda}\Big[\boldsymbol{i}_1\boldsymbol{i}_1 - \frac{1}{2}(\boldsymbol{i}_2\boldsymbol{i}_2 + \boldsymbol{i}_3\boldsymbol{i}_3)\Big]. \tag{32}$$

We search the deformation gradient for plastic deformation $\mathbf{F}_{\rm i}$ is the form similar to Eq. (31),

$$\mathbf{F}_{\rm i} = \lambda_{\rm i}\boldsymbol{i}_1\boldsymbol{i}_1 + \frac{1}{\sqrt{\lambda_{\rm i}}}(\boldsymbol{i}_2\boldsymbol{i}_2 + \boldsymbol{i}_3\boldsymbol{i}_3). \tag{33}$$

Eq. (33) implies that

$$\mathbf{d}_{\rm i} = \frac{\dot\lambda_{\rm i}}{\lambda_{\rm i}}\Big[\boldsymbol{i}_1\boldsymbol{i}_1 - \frac{1}{2}(\boldsymbol{i}_2\boldsymbol{i}_2 + \boldsymbol{i}_3\boldsymbol{i}_3)\Big]. \tag{34}$$

The deformation gradient for elastic deformation is given by

$$\mathbf{F}_{\rm e} = \lambda_{\rm e}\boldsymbol{i}_1\boldsymbol{i}_1 + \frac{1}{\sqrt{\lambda_{\rm e}}}(\boldsymbol{i}_2\boldsymbol{i}_2 + \boldsymbol{i}_3\boldsymbol{i}_3), \tag{35}$$

where $\lambda_{\rm e}$ stands for the elongation ratio for elastic deformation. The corresponding tensor $\mathbf{D}_{\rm e}$ is determined by the formula

$$\mathbf{D}_{\rm e} = \frac{\dot\lambda_{\rm e}}{\lambda_{\rm e}}\Big[\boldsymbol{i}_1\boldsymbol{i}_1 - \frac{1}{2}(\boldsymbol{i}_2\boldsymbol{i}_2 + \boldsymbol{i}_3\boldsymbol{i}_3)\Big]. \tag{36}$$

It follows from Eqs. (13) and (35) that

$$\mathbf{C}_{\rm e} - \frac{1}{3}I_{\rm e1}\mathbf{I} = \frac{2}{3}\Big(\lambda_{\rm e}^2 - \frac{1}{\lambda_{\rm e}}\Big)\Big[\boldsymbol{i}_1\boldsymbol{i}_1 - \frac{1}{2}(\boldsymbol{i}_2\boldsymbol{i}_2 + \boldsymbol{i}_3\boldsymbol{i}_3)\Big].$$

Inserting this expression and Eq. (34) into Eq. (25), we arrive at the differential equation

$$\frac{\dot\lambda_{\rm i}}{\lambda_{\rm i}} = \mathcal{P}V\frac{\lambda_{\rm e}^3 - 1}{\lambda_{\rm e}}, \tag{37}$$

where

$$V = \Big[1 - \frac{1}{K}\Big(\lambda_{\rm e}^2 + \frac{2}{\lambda_{\rm e}} - 3\Big)\Big]^{-1}. \tag{38}$$

Eqs. (10), (34) and (35) imply that $\mathbf{D}_{\rm i} = \mathbf{d}_{\rm i}$. Substitution of this equation and Eqs. (32), (34), (36) into Eq. (12) yields

$$\frac{\dot\lambda_{\rm e}}{\lambda_{\rm e}} = (1-\phi)\frac{\dot\lambda}{\lambda} - \mathcal{P}V\frac{\lambda_{\rm e}^3 - 1}{\lambda_{\rm e}}. \tag{39}$$

It follows from Eqs. (13), (23) and (35) that

$$\boldsymbol{\Sigma} = \Sigma_1\boldsymbol{i}_1\boldsymbol{i}_1 + \Sigma_2(\boldsymbol{i}_2\boldsymbol{i}_2 + \boldsymbol{i}_3\boldsymbol{i}_3), \tag{40}$$

where

$$\Sigma_1 = -\Pi + GV(1-\phi)\lambda_{\rm e}^2, \qquad \Sigma_2 = -\Pi + GV(1-\phi)\lambda_{\rm e}^{-1}.$$

According to the equilibrium equation and the boundary condition in stresses at the lateral surface of a sample,

$$\Sigma_2 = 0.$$

These relations imply that

$$\Sigma_1 = G(1-\phi)V(\lambda_{\rm e}^2 - \lambda_{\rm e}^{-1}).$$

Introducing the engineering tensile stress

$$\sigma = \frac{\Sigma_1}{\lambda}, \tag{41}$$

we find that

$$\sigma = G(1-\phi)V\frac{\lambda_{\rm e}^3 - 1}{\lambda\lambda_{\rm e}}. \tag{42}$$

Eqs. (39) and (42) provide governing equations for uniaxial tension of a supramolecular elastomer with an arbitrary deformation program $\lambda(t)$.

It follows from Eqs. (26), (27) and (32) that the function ϕ obeys the equation

$$\dot\phi = \frac{a(1-\phi)^2}{\lambda_{\rm e}^2 + 2\lambda_{\rm e}^{-1}}\sqrt{\frac{3}{2}}\frac{\dot\lambda}{\lambda}. \tag{43}$$

Bearing in mind that the coefficient $\mathcal{P}$ in Eq. (39) vanishes under tension, we conclude that Eqs. (39) and (43) form a set of two differential equations for $\lambda_{\rm e}$. At small strains, when $\lambda = 1+\epsilon$ and $\lambda_{\rm e} = 1+\epsilon_{\rm e}$ with $|\epsilon|, |\epsilon_{\rm e}| \ll 1$, these relations are simplified,

$$\dot\phi = \frac{a}{\sqrt{6}}(1-\phi)^2\dot\epsilon, \qquad \dot\epsilon_{\rm e} = (1-\phi)\dot\epsilon. \tag{44}$$

It follows from Eq. (44) that

$$\frac{{\rm d}\phi}{{\rm d}\epsilon_{\rm e}} = \frac{a}{\sqrt{6}}(1-\phi). \tag{45}$$

The physical meaning of Eq. (26) can be explained with the help Eq. (45). This relation shows that ϕ grows exponentially with elastic strain (at least, at small deformations) until it reaches the ultimate value. The coefficient $I_{\rm e1}$ is introduced into Eq. (26) to account for slowing down of the slippage process induced by orientation of chains at large deformations.

Under tension (compression) with a constant strain rate $\dot\epsilon$,

$$\lambda = 1 + \dot\epsilon t, \tag{46}$$

Eqs. (39), (42) and (43) with $\mathcal{P} = 0$ provide a closed set of the stress–strain relations. An advantage of these equations is that they involve only three (for the Gent model (21)) or two (for the neo-Hookean model (22)) material constants.

Under cyclic tensile deformation with a constant strain rate $\dot\epsilon$ and a maximum elongation ratio λ^*, the coefficient $\mathcal{P}$ in Eq. (39) vanishes under loading and adopts a non-zero value under retraction,

$$\mathcal{P} = P\exp\Big[-\alpha(\sigma^*\lambda^* - \sigma\lambda)\Big], \tag{47}$$

where σ^* is the maximum tensile stress under loading. As Eq. (47) contains two coefficients, P and α, the number of material parameters in the model increases up to four (for the neo-Hookean model) or five (for the Gent model). This number is substantially lower than that in previous constitutive models for the mechanical response of supramolecular elastomers.

3. Fitting of experimental data

To examine the ability of the model to describe experimental data under tension, compression and cyclic loading with large deformations, we analyze several sets of experimental data on supramolecular elastomers with various types of dynamic bonds. Compositions of the elastomers and their preparation procedures are described in Sect. S-1 (Supplementary Information). An algorithm for matching the stress–strain diagrams is provided in Sect. S-2. The experimental data depicted in Figs. 1 to 9, 10 and 12 are used to determine material parameters and to assess how they evolve when the structure of elastomers or external conditions are varied. The data presented in Fig. 13 are employed for validation of the model.

3.1. The neo-Hookean model

First, we fit stress–strain curves that do not involve intervals of stress-hardening. These diagrams are described by the neo-Hookean model (22) with two parameters (G and a) under uniaxial tension (compression) and four parameters (G, a, P and α) under cyclic deformation.

3.1.1. PDMS-based elastomers with several types of reversible bonds

We begin with matching the stress–strain curves on poly(dimethylsiloxane) (PDMS)-based supramolecular elastomers (Li et al., 2021a) with dynamic covalent disulfide bonds (PDMS-HEDS), double and quadruple hydrogen bonds (PDMS-UPy), disulfide and hydrogen bonds (PDMS-HEDS-UPy) and covalent and double hydrogen bonds (PDMS-HDO). Experimental data in uniaxial tensile tests (up to breakage of samples) are depicted in Fig. 1A together with results of simulation with the material constants collected in Tab. S-1.

Fig. 1A and Tab. S-1 show that the elastomer with only disulfide bonds is rather weak. Replacement of disulfide bonds with double and quadruple hydrogen bonds results in a pronounced (by a factor of five) increase in the shear modulus G. Simultaneous introduction of disulfide and hydrogen bonds results in an increase in stiffness by twice and leads to a weak reduction (by 25%) in the rate of plastic flow a. A similar reduction in a (by 22%) is observed when disulfide bonds are replaced with covalent and double hydrogen bonds.

For all elastomers under consideration, elongation to break $\epsilon_{\rm b}$ is weakly affected by the chemistry of supramolecular bonds and lies in

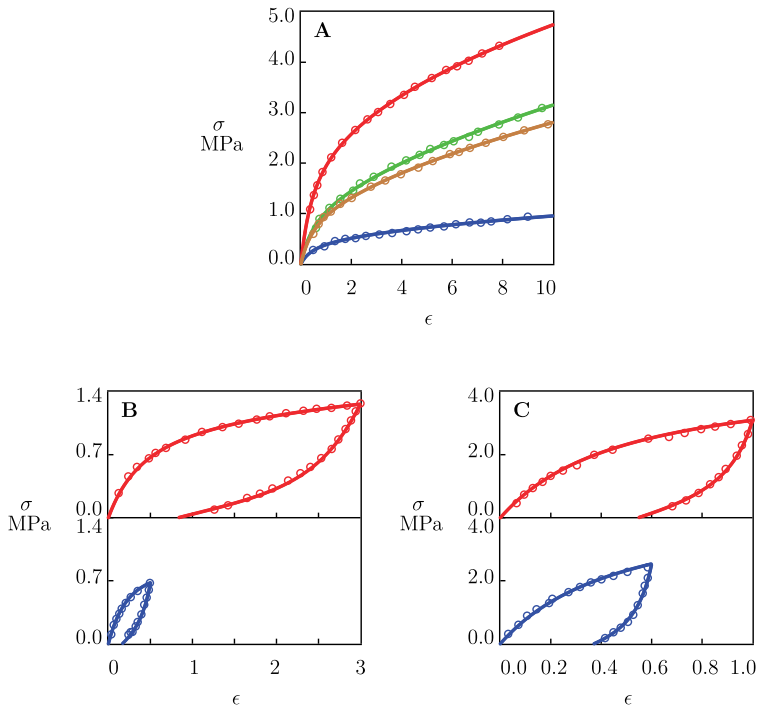

Fig. 1. Tensile stress σ versus tensile strain ϵ. A – Circles: experimental data (Li et al., 2021a) on PDMS elastomers with covalent cross-links (PDMS-HDO, brown), disulfide bonds (PDMS-HEDS, blue), hydrogen bonds (PDMS-UPy, red), and disulfide and hydrogen bonds (PDMS-HEDS-UPy, green) in tensile tests with strain rate $\dot{\epsilon} = 0.0167$ s^{-1}. B – Circles: experimental data (Li et al., 2021a) on PDMS-HEDS-UPy elastomer in cyclic tensile tests with strain rate $\dot{\epsilon} = 0.0167$ s^{-1} and various maximum strains ϵ_{max} (blue – $\epsilon_{max} = 0.5$, red – $\epsilon_{max} = 3.0$). C – Circles: experimental data (Wu et al., 2019b) on elastomer HHM-PAA-$Zn_{0.5}$ in cyclic tensile tests with strain rate $\dot{\epsilon} = 0.0042$ s^{-1} and various maximum strains ϵ_{max} (blue – $\epsilon_{max} = 0.6$, red – $\epsilon_{max} = 1.0$). Solid lines: results of numerical analysis.

the interval between 8 and 10. Some increase in ϵ_b may be mentioned for polymer networks with double hydrogen bonds.

Experimental data in cyclic tensile tests (with maximum strains 0.5 and 3.0) on elastomer PDMS-HEDS-UPy with disulfide and hydrogen bonds are reported in Fig. 1B together with results of numerical analysis with the material parameters listed in Tab. S-2.

Comparison of Tabs. S-1 and S-2 shows that the elastic modulus G adopts similar values (0.95, 1.0 and 1.2 MPa), whereas the rate of viscoplastic flow a changes noticeably (from 0.8 to 3.5), which may be explained by inaccuracy of measurements. Tab. S-2 demonstrates that an increase in the maximum strain ϵ_{max} induces a pronounced (by a factor of 19) decay in the coefficients P and a weakly reduction in the coefficients α.

For comparison, we match experimental data (Wu et al., 2019b) on supramolecular elastomer HHM-PAA-$Zn_{0.5}$ (a copolymer of HEMA, HEA, MAA and PAA physically cross-linked by ionic complexes between Zn^{2+} ions and carboxyl groups of PAA). Observations in cyclic tensile tests with maximum strains $\epsilon_{max} = 0.6$ and 1.0 are presented in Fig. 1C together with results of numerical analysis with the material parameters collected in Tab. S-2. This table shows that an increase in ϵ_{max} by a factor of 1.7 results in a decrease in P and α by factors 2.5 and 2.0, respectively.

To evaluate the effect of strain rate $\dot{\epsilon}$ on the shear modulus G and the rate of viscoplastic flow a, we approximate experimental data on elastomer PDMS-HEDS-UPy in tensile tests with $\dot{\epsilon}$ ranged from 0.0167 to 0.167 s^{-1}. Experimental stress–strain diagrams (Li et al., 2021a) are depicted in Fig. 2A together with results of simulation. Evolution of the material parameters with strain rate is illustrated in Fig. 2B, where the data are approximated by the equations

$$G = G_0 + G_1 \log \dot{\epsilon}, \qquad a = a_0 + a_1 \log \dot{\epsilon}, \tag{48}$$

where $\log = \log_{10}$, and the coefficients are determined by the least-squares method. This figure shows that G increases noticeably (by a factor of 1.7), whereas the growth of a with the strain rate is rather modest (by 15%).

An increase in the elastic modulus with strain rate in covalently cross-linked elastomers is conventionally associated with relaxation of stresses (substantial under slow loading and insignificant under rapid stretching). This explanation is not applicable, however, to supramolecular elastomers whose viscoelasticity is negligible. We hypothesize that an increase in G observed in Fig. 2B is driven by the presence of entanglements between chains. Under loading with low strain rates, entangled chains have sufficient time to slide with respect to each other. As a consequence, appropriate segments of chains remain dangling, and their contribution to the elastic energy can be disregarded. Under rapid stretching, chains have no time to slip with respect to each other at the entanglement points. Their segments connected by entanglements become active (stressed), and their contribution into the mechanical energy becomes noticeable. This contribution is reflected by the growth in the elastic modulus with strain rate.

3.1.2. PAA-based elastomers with ionic bonds

To examine how entanglements affect the viscoplastic response of supramolecular polymers, we analyze experimental data (Wu et al., 2019b) on a series of HHM-PAA-$Zn_{\frac{1}{n}}$ elastomers (n stands for the molar ratio of carboxyl groups of PAA chains to Zn^{2+} ions) in uniaxial tensile and compressive tests. Chains in the polymer networks are connected by ionic complexes between mobile Zn^{2+} ions and ionized carboxyl groups of poly(acrylic acid) (PAA) chains.

Observations in tensile and compressive tests (up to breakage of samples) are depicted in Figs. 3A and 3B, respectively. The data are presented together with results of numerical analysis. The best-fit material parameters are reported in Fig. S-1, where they are plotted versus n. Evolution of the coefficients G and a with n is described by the linear equations

$$G = G_0 + G_1 n, \qquad a = a_0 + a_1 n \tag{49}$$

with the coefficients calculated by the least-squares algorithm. Fig. S-1 shows that G and a increase with n, but the data for $n = 2$

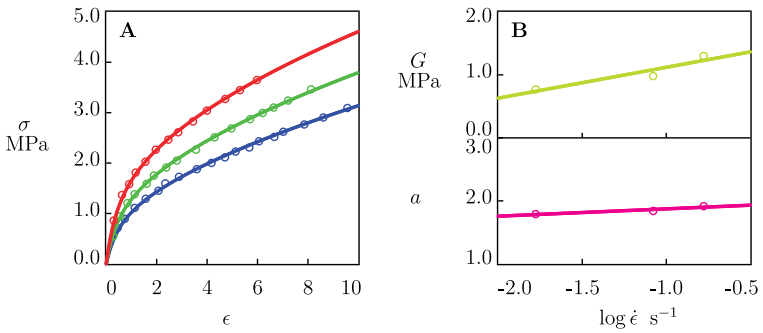

Fig. 2. A – Tensile stress σ versus tensile strain ϵ. Circles: experimental data (Li et al., 2021a) on PDMS-HEDS-UPy elastomer in tensile tests with various strain rates $\dot{\epsilon}$ (blue – $\dot{\epsilon} = 0.0167$, green – $\dot{\epsilon} = 0.0835$, red – $\dot{\epsilon} = 0.167$ s^{-1}). Solid lines: results of numerical analysis. B – Parameters G and a versus strain rate $\dot{\epsilon}$. Circles: treatment of experimental data. Solid lines: results of simulation.

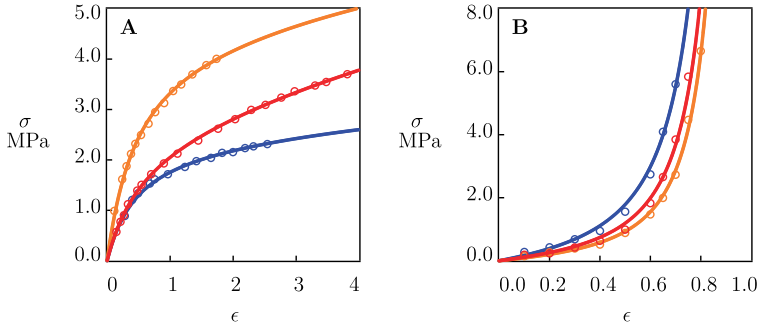

Fig. 3. A – Tensile stress σ versus tensile strain ϵ. B – Compressive stress σ versus compressive strain ϵ. Circles: experimental data (Wu et al., 2019b) on elastomers HHM-PAA-$Zn_{0.3}$ (blue), HHM-PAA-$Zn_{0.5}$ (orange) and HHM-PAA-$Zn_{0.6}$ (red) in tensile tests with strain rate $\dot{\epsilon} = 0.0042$ s^{-1} and compressive tests with strain rate $\dot{\epsilon} = 0.0021$ s^{-1}. Solid lines: results of numerical analysis.

(corresponding to the stoichiometric condition when all Zn^{2+} ions form reversible cross-links between polymer chains) deviate noticeably from the theoretical curves.

Fig. S-1 demonstrates that the responses under tension and compression are strongly asymmetric. The viscoplastic flow is noticeable under tension (the coefficient a ranges from 0.9 to 1.5), but it becomes negligible under compression (all diagrams in Fig. 3B are matched with $a = 0$). The shear modulus G under tension exceeds strongly (by a factor of 3) that under compression.

This asymmetry can be explained by the role that entanglements play in transmission of external load. Under tension, most of the entanglements act as permanent cross-links. Segments of chains bridged by entanglements remain active, and stresses in these segments contribute to the total tensile stress σ. Slippage of active segments with respect to each other at the entanglement points induces the viscoplastic flow in the elastomer at the macroscopic level. On the contrary, segments of chains linked by entanglements are dangling under compression. As stresses in dangling segments vanish, these segments do not contribute to the elastic energy (G is reduced strongly) and the viscoplastic flow (a vanishes).

3.1.3. SIS-based elastomers with covalent and ionic bonds

To evaluate further the role of ionic bonds between chains, we study experimental data (Kajita et al., 2022) in tensile and compressive tests on poly(styrene–isoprene–styrene) (SIS)-based supramolecular elastomers. Chains in the polymer networks are permanently cross-linked by polystyrene domains (arising due to phase separation) and ionic bonds between mobile ions (Ba^{2+} or Na^{+} in elastomers SIS-Ba and SIS-Na, respectively) and carboxyl groups of SIS chains functionalized with maleic anhydride.

We begin with fitting observations in tensile tests with various strain rates $\dot{\epsilon}$ on SIS-Ba elastomer (Kajita et al., 2022). Experimental stress–strain diagrams under tension (up to breakage of samples) with $\dot{\epsilon}$ ranged from 0.01 to 1.0 s^{-1} are reported in Fig. 4A together with results of numerical analysis. Material parameters G and a are presented in Fig. 4C which confirms the ability of Eqs. (48) to approximate the data. The parameters G and a increase noticeably with the strain rate, in accord with the results depicted in Fig. 2B for the elastomer with another type of reversible bonds.

Experimental data (Kajita et al., 2022) on SIS-Ba elastomer in compressive test with the strain rate $\dot{\epsilon} = 0.1$ s^{-1} are depicted in Fig. 5A together with results of simulation with the material coefficients listed in Tab. S-3.

3.2. The Gent model

We now focus on matching experimental data on supramolecular elastomers revealing stress-hardening at the final stage of tension. Their stress–strain diagrams are described by the Gent model (21) with three parameters (G, a and K) under tension and five parameters under cyclic deformation.

3.2.1. SIS-based elastomers with covalent and van der Waals bonds

We begin with matching experimental data on SIS-Na elastomer whose chains are connected by covalent cross-links (arising due to phase separation of styrene segments) and van der Waals forces between dipoles formed by Na^{+} ions and ionized carboxyl groups. The latter complexes are stronger than the complexes formed by bulky Ba^{2+} ions, but their concentration is substantially lower than that in SIS-Ba elastomer (Kajita et al., 2022).

Experimental data (Kajita et al., 2022) on SIS-Na elastomer in tensile tests with various strain rates $\dot{\epsilon}$ are reported in Fig. 4B. The effect of strain rate on material parameters G, a and K is illustrated in Fig. 4D. The data are approximated by Eq. (48) and the equation

$$\log K = K_0 + K_1 \log \dot{\epsilon}, \tag{50}$$

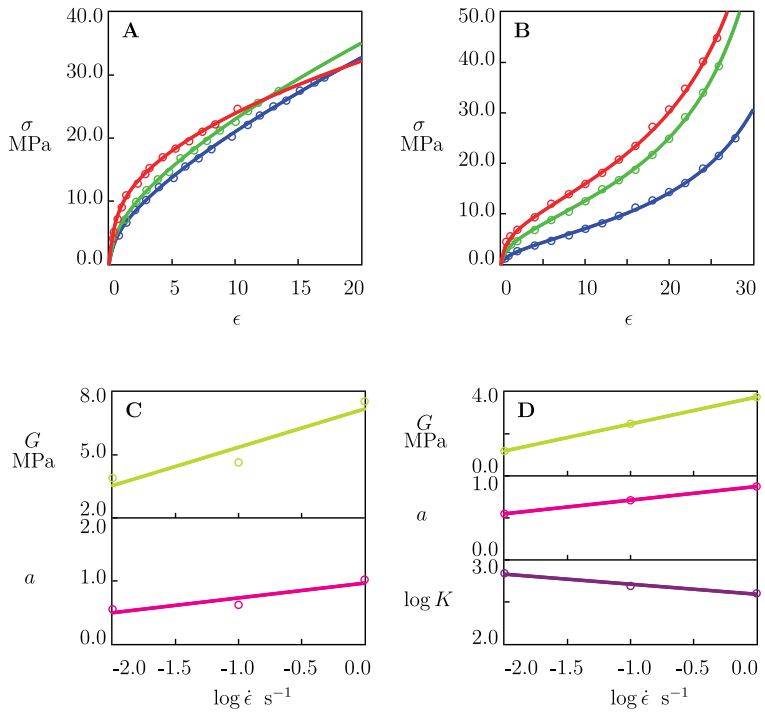

Fig. 4. A, B – Tensile stress σ versus tensile strain ϵ. Circles: experimental data (Kajita et al., 2022) on SIS-Ba (A) and SIS-Na (B) elastomers in tensile tests with various strain rates $\dot{\epsilon}$ (blue – $\dot{\epsilon} = 0.01$, green – $\dot{\epsilon} = 0.1$, red – $\dot{\epsilon} = 1.0$ s^{-1}). C, D – Parameters G, a and K versus strain rate $\dot{\epsilon}$. Circles: treatment of experimental data on SIS-Ba (C) and SIS-Na (D) elastomers. Solid lines: results of numerical analysis.

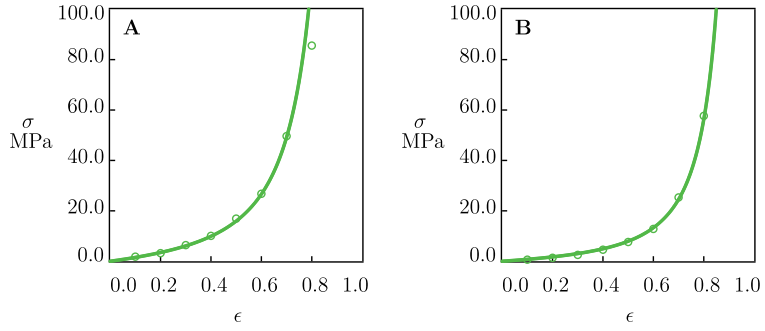

Fig. 5. A, B – Compressive stress σ versus compressive strain ϵ. Circles: experimental data (Kajita et al., 2022) on SIS–Ba (A) and SIS-Na (B) elastomers in tests with strain rate $\dot{\epsilon} = 0.1$ s^{-1}. Solid lines: results of numerical analysis.

where K_0 and K_1 are calculated by the least-squares technique.

Comparison of Figs. 4C and 4D shows that a adopt similar values for SIS-Na and SIS-Ba elastomers, whereas the shear modulus G of SIS-Ba elastomer exceeds that of SIS-Na elastomer by twice for all strain rates under consideration.

Observations on SIS-Na elastomer in compressive test with the strain rate $\dot{\epsilon} = 0.1$ s^{-1} (Kajita et al., 2022) are reported in Fig. 5B together with results of numerical analysis with the material parameters collected in Tab. S-3.

Table S-3 confirms the conclusion regarding the tension–compression asymmetry in supramolecular elastomers. In accord with Fig. S-1, this table shows that the viscoplastic flow vanishes ($a = 0$) under compression of SIS-Ba and SIS-Na elastomers, and their shear moduli G under tension exceed those under compression by 2 and 9%, respectively.

3.2.2. PDMS-based elastomers with hydrogen and metal–amine coordination bonds

We proceed with matching stress–strain diagrams on a series of PDMS-based elastomers cross-linked by quadruple hydrogen bonds between 2,4′-toluene diisocyanate (TDI) segments and metal–ligand coordination bonds between mobile Al^{3+} ions and TDI ligands (Wu et al., 2019a).

Experimental data in tensile tests with a fixed strain rate $\dot{\epsilon}$ (up to breakage of samples) in elastomers PDMS-TDI-Al$_{\frac{1}{n}}$ (with $n = 1$, 2 and 4 standing for the TDI:Al molar ratio) are reported in Fig. 6A together with results of numerical analysis. Each set of observations is matched by means of three coefficients, G, a and K. The parameters G, a and K are plotted versus n in Fig. 6C, where the data are approximated by Eq. (49) and the equation

$$\log K = K_0 + K_1 n \tag{51}$$

with the coefficients K_0, K_1 determined by the least-squares method.

Observations in tensile tests with various strain rates $\dot{\epsilon}$ (ranging from 0.008 to 0.067 s^{-1}) on elastomer PDMS-TDI-Al$_{\frac{1}{3}}$ are plotted in

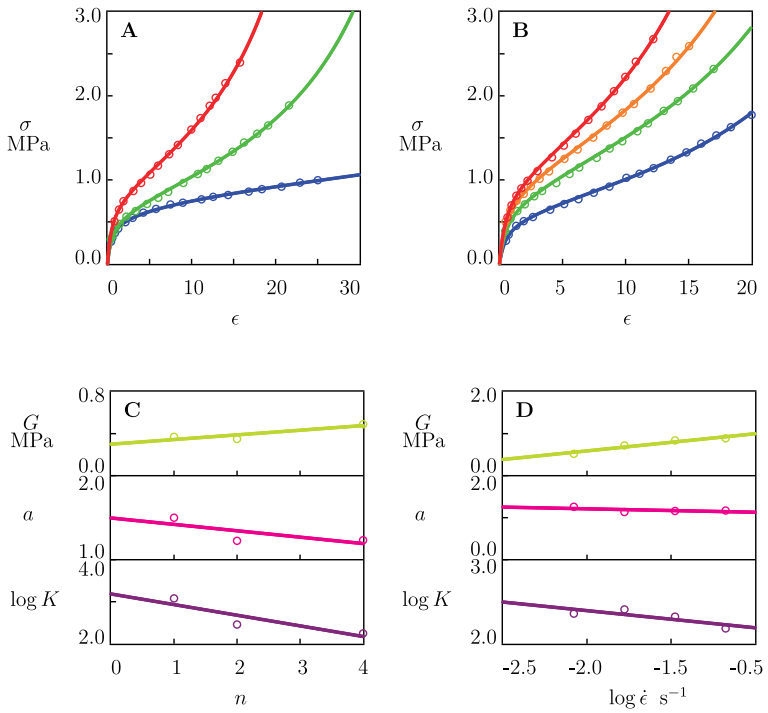

Fig. 6. A, B – Tensile stress σ versus tensile strain ϵ. Circles: experimental data (Wu et al., 2019a). A – PDMS-TDI-Al$_{\frac{1}{n}}$ elastomers with various TDI:Al molar ratios n in tensile tests with strain rate $\dot{\epsilon} = 0.0167$ s^{-1} (blue – $n = 1$, green – $n = 2$, red – $n = 4$). B – PDMS-TDI-Al$_{\frac{1}{3}}$ elastomer in tensile tests with various strain rates $\dot{\epsilon}$ (blue – $\dot{\epsilon} = 0.0084$, green – $\dot{\epsilon} = 0.0167$, orange – $\dot{\epsilon} = 0.0334$, red – $\dot{\epsilon} = 0.0668$ s^{-1}). C – Parameters G, a and K versus n. D – Parameters G, a and K versus $\dot{\epsilon}$. Circles: treatment of experimental data. Solid lines: results of numerical analysis.

Fig. 6B together with results of simulation. The effect of strain rate of the coefficients G, a and K is illustrated in Fig. 6D, where the data are approximated by Eqs. (48) and (50). Unlike Figs. 2B, 4C and 4D that reveal an increase in a with $\dot{\epsilon}$, Fig. 6D shows that the rate of viscoplastic flow a decreases weakly with strain rate.

3.2.3. PU-based elastomers with catechol–boronic ester bonds

We now fit experimental data (Yang et al., 2020) on a series of polyurethane (PU)-based elastomers permanently cross-linked with two types of chain extenders (dopamine-derived diol (DADO) and 1,4-butanediol) and reversible bonded with catechol–boronic ester linkages (with various densities of reversible bonds and various fractions of free catechol moieties).

Elastomers of the N-X-0 series were prepared from linear polyurethanes with various ratios X of DADO and 1,4-butanediol as chain extenders and 1:1 molar ratio of boronic acid to catechol. Elastomers of the N-X-Y series were prepared from linear polyurethane (with DADO as the only chain extender) with various molar ratios X of boronic acid groups to catechol groups and molar fractions Y of 1,4-phenylenediboronic acid (X, Y are given in per cent).

Stress–strain diagrams on several elastomers N-X-Y under uniaxial tension with a fixed strain rate $\dot{\epsilon}$ (up to breakage of specimens) are presented in Fig. 7 together with results of numerical analysis with the material parameters collected in Tab. S-4. This table shows that an increase in molar fraction of DADO results in a noticeable (by a factor of 3) increase in the shear modulus G and a pronounced (by a factor of 14) decay in the rate of viscoplastic flow a. An increase in the molar fraction of 1,4-phenylenediboronic acid leads to a strong growth (by 4 to 7 times) of the shear modulus G and noticeable (by a factor of 1.2 to 2) increase in the coefficient K, but it does not affect practically the rate of viscoplastic flow a.

To evaluate how composition of PU-based elastomers affects their response under cyclic loading, we fit observations on elastomers N-70-30 and N-70-00 in cyclic tensile tests with the strain rate $\dot{\epsilon} = 0.033$ s^{-1} and maximum strain $\epsilon_{\max} = 2$. The experimental stress–strain diagrams are depicted in Fig. 8A together with results of numerical analysis with the material constants listed in Tab. S-5. This table shows that the presence of catechol–boronic ester bonds induces a strong (by a factor of 2.8) increase in the shear modulus G, an appropriate reduction (by 40%) of the rate of viscoplastic flow a, and a pronounced (by a factor of 5) increase in the coefficient K. The effect of these bonds on the response under retraction is rather modest: the rate of viscoplastic flow P decreases by 15% only.

For comparison, experimental data (Wu et al., 2019a) are matched on PDMS-based elastomers, PDMS-TDI-Al$_{\frac{1}{3}}$ and PDMS-IP-Al$_{\frac{1}{3}}$, in cyclic tensile tests with the strain rate $\dot{\epsilon} = 0.0167$ s^{-1} and maximum strain $\epsilon_{\max} = 11.4$. The difference between PDMS-TDI-Al$_{\frac{1}{3}}$ and PDMS-IP-Al$_{\frac{1}{3}}$ is that TDI segments form quadruple H-bonds, while IP segments form double H-bonds. Experimental stress–strain diagrams are depicted in Fig. 8B together with results of simulation with the material parameters reported in Tab. S-5.

Tab. S-5 demonstrates that enhancement of strong (catechol–boronic ester) bonds affects noticeably the response of elastomers under stretching and does not influence their behavior under retraction, whereas enhancement of weak (hydrogen) bonds causes the inverse effect: the mechanical response under tension remains practically unaffected, while the rate of viscoplastic flow at unloading increases by 60%.

3.2.4. PDMS-based elastomers with hydrogen and metal–pyridine bonds

We now fit experimental data (Fan et al., 2021) on a series of PDMS-based elastomers PDMS-DAP-Fe$_{\frac{1}{n}}$ ($n = 1, \dots, 5$ stands for the DAP:Fe molar ratio) bonded by metal–ligand coordination complexes between Fe^{3+} ions and pyridine groups of DAP and H-bonds between pyridine and urea groups.

Observations in tensile tests with a fixed strain rate $\dot{\epsilon}$ (up to breakage of samples) on elastomers PDMS-DAP-Fe$_{\frac{1}{n}}$ are depicted in Fig. 9A together with results of numerical analysis. Each set of data is matched by means of three coefficients, G, a and K. These parameters are plotted

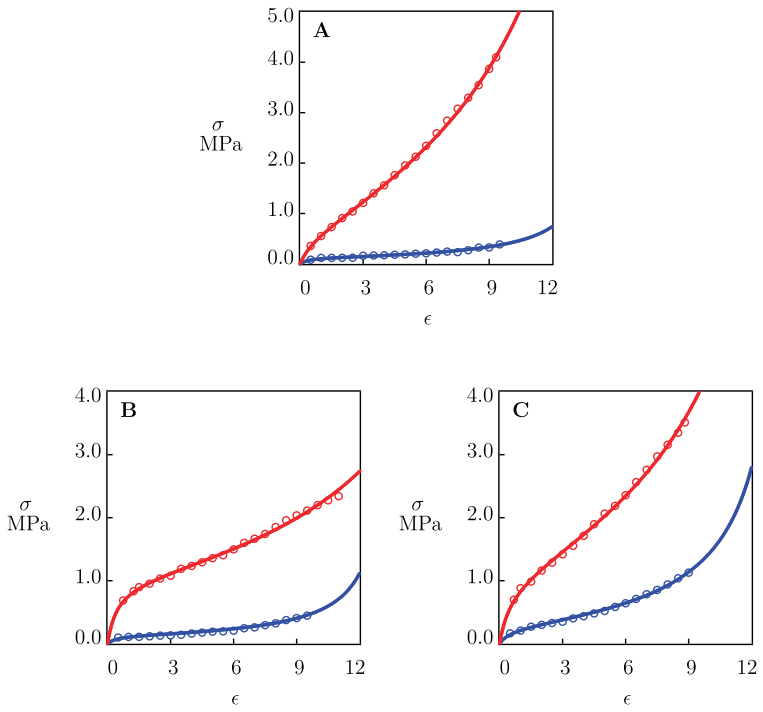

Fig. 7. Tensile stress σ versus tensile strain ϵ. Circles: experimental data (Yang et al., 2020) on PU elastomers in tensile tests with strain rate $\dot{\epsilon} = 0.033$ s^{-1} (A: blue – N-50-00, red – N-100-00, B: blue – N-50-00, red – N-50-50, C: blue – N-70-00, red – N-70-30). Solid lines: results of numerical analysis.

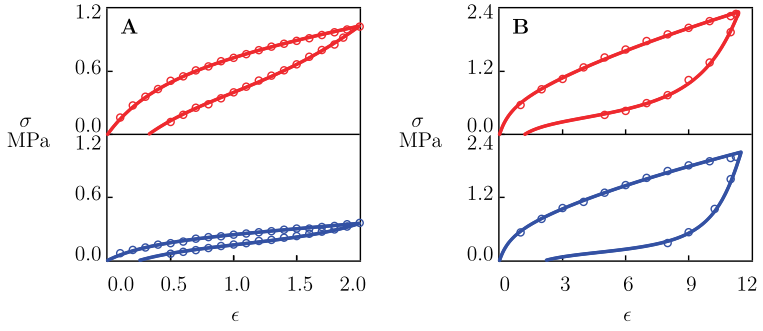

Fig. 8. Tensile stress σ versus tensile strain ϵ. A – Circles: experimental data (Yang et al., 2020) on N-70-30 (red) and N-70-00 (blue) elastomers in cyclic tests with strain rate $\dot{\epsilon} = 0.033$ s^{-1} and maximum strain $\epsilon_{max} = 2.0$. B – Circles: experimental data (Wu et al., 2019a) on PDMS-TDI-Al$_3$ (red) and PDMS-IP-Al$_3$ (blue) elastomers in cyclic tests with strain rate $\dot{\epsilon} = 0.0167$ s^{-1} and maximum strain $\epsilon_{max} = 11.4$. Solid lines: results of numerical analysis.

versus n in Fig. 9C, where the data are approximated by Eq. (49) and (51). Fig. 9C shows that G decreases linearly with n, whereas a and K remain practically independent of the DAP:Fe molar ratio.

Comparison of Figs. 6C and 9C shows that G increases with n for PDMS-TDI-Al$_{\frac{1}{n}}$ elastomers and decreases for PDMS-DAP-Fe$_{\frac{1}{n}}$ elastomers. This difference between the effect of n (the molar ratio of ligands to metal ions) on the elastic modulus G may be explained by competition between hydrogen bonds and metal–ligand coordination linkages. For a fixed molar fraction of ligands in the composition of supramolecular polymers, an increase in n is tantamount to a reduction in density of coordination bonds and the corresponding increase in concentration of hydrogen bonds. When the strength of hydrogen bonds exceeds that of coordination bonds, G grows with n (Fig. 6C). On the contrary, when coordination bonds are stronger than H-bonds, G decreases with n (Fig. 9C).

To examine the influence of strain rate on the viscoplastic response of PDMS-based elastomers, we fit observations on PDMS-DAP-Fe$_{\frac{1}{3}}$ in tensile tests (up to breakage of specimens) with various strain rates $\dot{\epsilon}$ ranging from 0.012 to 0.208 s^{-1}. Experimental stress–strain diagrams are depicted in Fig. 9B together with results of numerical analysis. Each set of data is approximated by three material parameters, G, a and K. The effect of strain rate on these coefficients is illustrated in Fig. 9D, where the data are approximated by Eqs. (48) and (50). Fig. 9D shows that G increases substantially with $\dot{\epsilon}$, a remains practically independent of the strain rate, whereas K decreases with $\dot{\epsilon}$. Similar dependencies of the material parameters on strain rate are reported in Fig. 6D for PDMS-TDI-Al$_{\frac{1}{n}}$ elastomers.

4. Discussion

Analysis of experimental data on supramolecular elastomers (Figs. 1 to 9) in tensile and compressive tests with various strain rates $\dot{\epsilon}$ and cyclic (loading–retraction) tests with various maximum strains ϵ_{max} confirms the ability of the model to describe the experimental stress–strain curves under finite deformations (with elongation ratios up to 30). Figs. 2B, 4C, 4D, 6D and 9D show that the effect of strain rate on material parameters is adequately predicted by Eqs. (48) and (50). Given compositions of the elastomers under consideration, Eqs. (49) and (51) describe how these parameters are affected by concentration of supramolecular bonds between chains (Figs. 6C, 9C and Tabs. S-1, S-4, S-5).

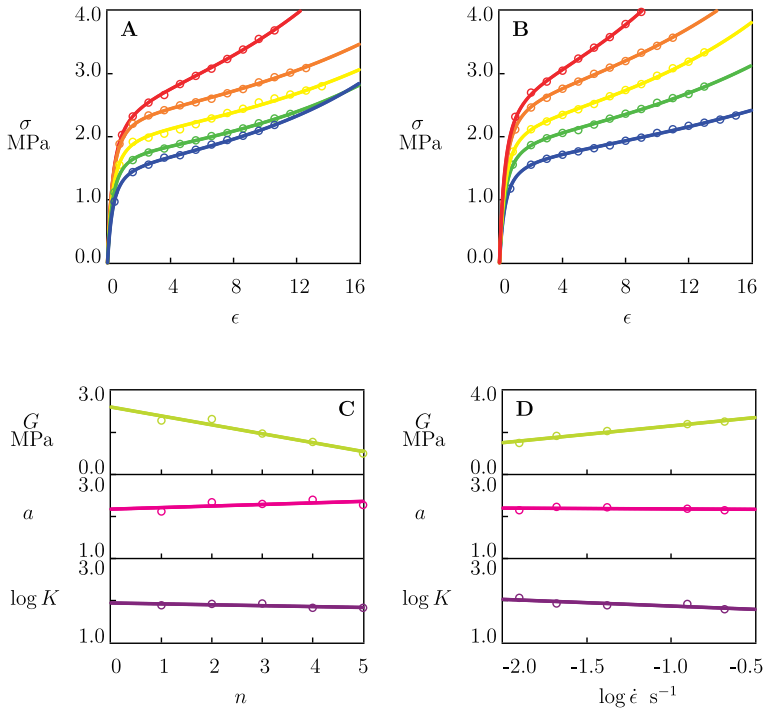

Fig. 9. A, B – Tensile stress σ versus tensile strain ϵ. Circles: experimental data (Fan et al., 2021). A – PDMS-DAP-Fe$_{\frac{1}{n}}$ elastomers with various DAP:Fe molar ratios n in tensile tests with strain rate $\dot{\epsilon} = 0.208$ s^{-1} (blue – $n = 1$, green – $n = 2$, yellow – $n = 3$, orange – $n = 4$, red – $n = 5$). B – PDMS-DAP-Fe$_{\frac{1}{3}}$ elastomer in tensile tests with various strain rates $\dot{\epsilon}$ (blue – $\dot{\epsilon} = 0.013$, green – $\dot{\epsilon} = 0.021$, yellow – $\dot{\epsilon} = 0.042$, orange – $\dot{\epsilon} = 0.125$, red – $\dot{\epsilon} = 0.208$ s^{-1}). C – Parameters G, a and K versus n. D – Parameters G, a and K versus $\dot{\epsilon}$. Circles: treatment of experimental data. Solid lines: results of numerical analysis.

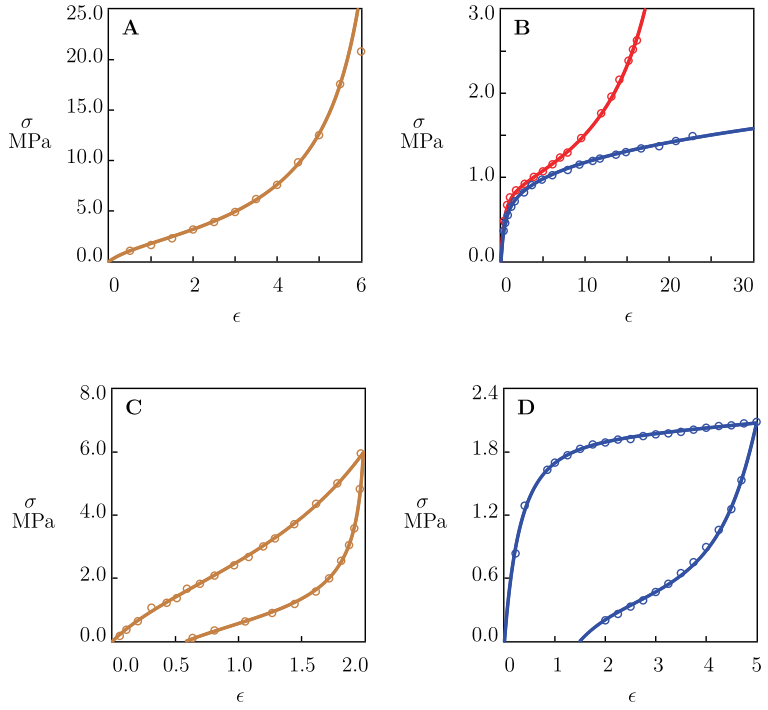

Fig. 10. Tensile stress σ versus tensile strain ϵ. Circles: experimental data. Solid lines: results of numerical analysis. A – CB-filled butyl rubber in tensile test with strain rate $\dot{\epsilon} = 0.021$ s^{-1} (Yan et al., 2017). B – supramolecular elastomers PDMS-TDI-Al$_{\frac{1}{3}}$ (red) and PDMS-IP-Al$_{\frac{1}{3}}$ (blue) in tensile tests with strain rate $\dot{\epsilon} = 0.0167$ s^{-1} (Wu et al., 2019a). C – CB-filled styrene-butadiene rubber in cyclic tensile test with strain rate 0.333 s^{-1} and maximum strain $\epsilon_{max} = 2$ (Plagge and Kluppel, 2019). D – supramolecular elastomer PDMS-DAP-Fe$_{\frac{1}{3}}$ in cyclic tensile test with strain rate $\dot{\epsilon} = 0.021$ s^{-1} and maximum strain $\epsilon_{max} = 5.0$ (Fan et al., 2021).

To examine the difference between the responses of covalently cross-linked and supramolecular elastomers, we analyze the experimental data in Fig. 10. Figs. 10A and 10B show the stress–strain diagrams under uniaxial tension. Observations on butyl rubber reinforced with carbon black (Yan et al., 2017) and elastomers PDMS-TDI-Al$_{\frac{1}{3}}$ and PDMS-IP-Al$_{\frac{1}{3}}$ (Wu et al., 2019a) are chosen as typical examples. The data is approximated by the model with the material parameters reported in Tab. S-6.

The stress–strain diagram on vulcanized rubber (Fig. 10A) involves three intervals (corresponding to the nonlinear elastic response, strain-softening and stress-hardening) and terminates at a strain at break $\epsilon_b \approx 6$. The stress–strain curves on supramolecular elastomers (Fig. 10B) contain two or three (depending on the strength of secondary bonds between chains) intervals, and breakage of specimens occur at substantially higher strains $\epsilon_b = 20$ to 25. Bearing in mind that the shear moduli of the elastomers under consideration adopt similar values (Tab. S-6), the difference in shapes of the stress–strain diagrams is ascribed to the viscoplastic flow: its rate a vanishes for the butyl rubber and accepts relatively high values (belonging to the interval between 1.5 and 2.0) for the PDMS-based elastomers.

The neo-Hookean model fits experimental data in tensile tests on covalently cross-linked elastomers in a rather limited interval of strains (conventionally, below $\epsilon = 1$), where these materials demonstrate the nonlinear elastic behavior. Matching the stress–strain curves along the interval of strain-softening (induced by cavitation and growth of microvoids) requires more sophisticated models in hyperelasticity (Martins et al., 2006). The final interval of the stress–strain diagrams (where stress-hardening is driven by orientation of chains along the direction of loading and stress-induced crystallization) is conventionally predicted by the models accounting for finite extensibility of chains (Horgan and Saccomandi, 2006).

Unlike vulcanized rubbers, the mechanical behavior of supramolecular elastomers under tension can be described correctly by the neo-Hookean model at strains ϵ up to 25 (Fig. 10B), provided that the viscoplastic flow of junctions is taken into account.

The responses of vulcanized rubber and supramolecular elastomers in tensile loading–unloading tests are illustrated in Figs. 10C and 10D, where experimental data are presented on styrene-butadiene rubber reinforced with carbon black (Plagge and Kluppel, 2019) and elastomer PDMS-DAP-Fe$_{\frac{1}{3}}$ (Fan et al., 2021). The stress–strain curves are fitted by the model with the material parameters collected in Tab. S-7.

The diagrams under retraction in Figs. 10C and 10D have different shapes. They are characterized by a rapid decay in stress resulting in a relatively large residual strain for PDMS-based elastomer and a slow decrease in stress that leads to a small residual strain for styrene-butadiene rubber. This difference can be explained (Tab. S-7) by the difference in rates, a and P, of the viscoplastic flows under loading and unloading. The coefficient a vanishes for the vulcanized rubber and it adopts a relatively high value for the supramolecular elastomer. On the contrary, the coefficient P for styrene-butadiene rubber accepts a relatively large value exceeding that for the supramolecular elastomer by two orders of magnitude.

To evaluate how the mechanical behavior of covalently cross-linked elastomers differ from that of supramolecular elastomers under biaxial deformation, simulation is performed for equibiaxial tension with the deformation gradient

$$\mathbf{F} = \lambda(\boldsymbol{i}_1\boldsymbol{i}_1 + \boldsymbol{i}_2\boldsymbol{i}_2) + \lambda^{-2}\boldsymbol{i}_3\boldsymbol{i}_3,$$

where $\lambda = 1 + \epsilon$ stands for elongation ratio. The governing equations read

$$\sigma = G(1-\phi)\Big(1 - \frac{2\lambda_e^2 + \lambda_e^{-4} - 3}{K}\Big)^{-1}\frac{\lambda_e^6 - 1}{\lambda\lambda_e^4},$$
$$\frac{d\lambda_e}{d\lambda} = (1-\phi)\frac{\lambda_e}{\lambda},$$
$$\frac{d\phi}{d\lambda} = \frac{2a}{(2\lambda_e^2 + \lambda_e^{-4})\lambda}(1-\phi)^2, \tag{52}$$

where σ stands for the engineering stress. Eqs. (52) are developed by the same approach as Eqs. (39), (42) and (43) for uniaxial tension.

Stress–strain diagrams under uniaxial and equibiaxial deformations of vulcanized butyl rubber (Yan et al., 2017) and supramolecular elastomers N-100-00 (Yang et al., 2020), SIS(Na) and SIS(Ba) (Kajita et al., 2022) are reported in Fig. 11, where stress σ is plotted versus strain ϵ. Numerical analysis is conducted with the material parameters collected in Tabs. S-6, S-4 and Fig. 4, respectively.

For covalently cross-linked elastomers, the stress σ under equibiaxial tension exceeds that under uniaxial tension at all strains ϵ (Fig. 11A). A similar response (Fig. 11B) is revealed by highly cross-linked supramolecular elastomers (with low rates of plastic flow a). In this case, however, the stresses under uniaxial and equibiaxial deformations coincide practically along the intervals of strain-softening. When the rates of plastic flow a in supramolecular elastomers become relatively high (above 0.5), two types of the mechanical behavior are observed: (i) with stresses under equibiaxial tension exceeding those under uniaxial tension (except for some initial interval where plastic deformations are small), see Fig. 11C, and (ii) with stresses under uniaxial tension exceeding those under equibiaxial tension at very small and very large strain ϵ, see Fig. 11D. The stress–strain diagrams of the first type are typical for the elastomers with the neo-Hookean strain energy density, whereas the diagrams of the other type are characteristic for the elastomers with the Gent potential.

A characteristic feature of supramolecular elastomers (that distinguishes them from covalently cross-linked rubbers) is the tension–compression asymmetry: material parameters G and a found by fitting stress–strain curves under tension and compression adopt different (high for tension and low for compression) values (Fig. S-1 and Tab. S-3). This phenomenon is also observed in experiments on supramolecular hydrogels (Drozdov and deClaville Christiansen, 2020c). It can be explained by the fact that chains in supramolecular polymer networks are highly entangled (due to a large concentration of weak secondary bonds). Under tension, when all entanglements are active (segments of chains bridged by entanglements are stressed), they play the same role as cross-links between chains and contribute to the strain energy density of an elastomer. Under compression, part of entanglements become dangling (stresses vanish in segments connected by these entanglements), and the total contribution of entanglements to the strain energy density is reduced.

Although the model is derived in Section 2 for the response of supramolecular elastomers, it can be applied to describe observations on supramolecular gels as well. To verify this statement, experimental data are fitted on poly(acrylamide) gel dynamically cross-linked by host-guest bonds between 1-benzyl-3-vinylimidazolium and cucurbit[8]uril moieties (Liu et al., 2017).

Observations in uniaxial tensile tests with the strain rate $\dot{\epsilon} = 0.167\ s^{-1}$ are reported in Fig. 12 together with results of numerical simulation with the material constants collected in Tab. S-8. Fig. 12 shows reasonable agreement between the data and results of simulation at strains up to $\epsilon_b = 107$. Unlike supramolecular elastomers (for which the model reflects the physical picture of deformation), applicability of the model to supramolecular gels is merely phenomenological, as it does not account for viscoelasticity of these materials.

Application of the model to the description of the mechanical response of biological tissues (as another type of soft materials) requires modifications of the governing equations caused by replacement of the elastic potentials (21) and (22) with more sophisticated expressions (Federico et al., 2008; Chagnon et al., 2015; Mihai et al., 2017) and account for the anisotropy of their micro-structure.

To assess the ability of the model to predict experimental data on supramolecular elastomers under cyclic deformation, simulation is conducted for PDMS-based elastomer with disulfide and hydrogen bonds PDMS-HEDS-UPy under uniaxial tension–retraction with maximum strains under stretching $\epsilon_{max} = 1.0$, 1.5 and 2.0. Observations on this elastomer in cyclic tests with the strain rate $\dot{\epsilon} = 0.0167\ s^{-1}$ and

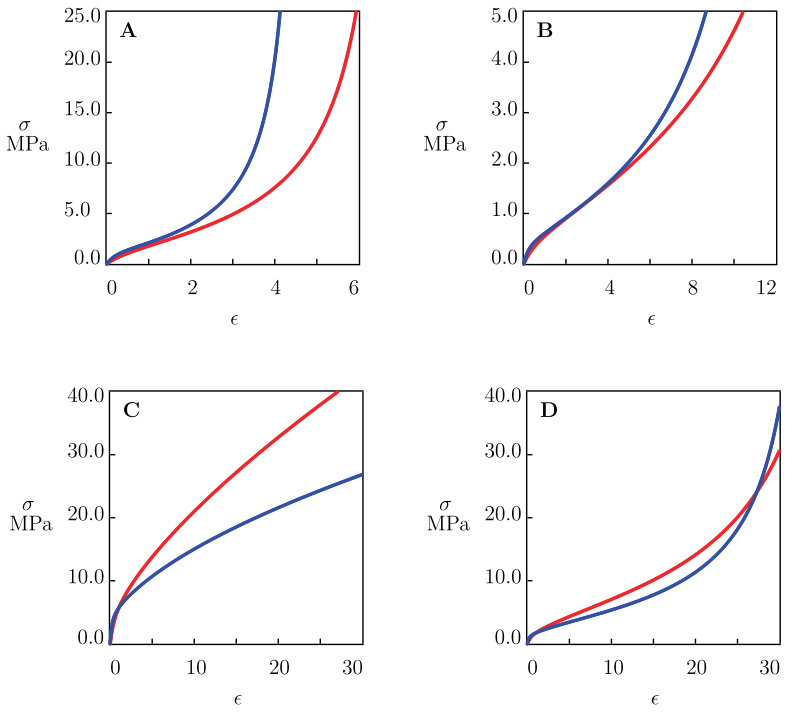

Fig. 11. Tensile stress σ versus tensile strain ϵ. Solid lines: results of numerical analysis for uniaxial (red) and equibiaxial (blue) tests. A – stretching of vulcanized butyl rubber with 25 phr of carbon black (Yan et al., 2017) with strain rate $\dot{\epsilon} = 0.021$ s^{-1}. B – stretching of polyurethane elastomer N-100-00 with strain rate $\dot{\epsilon} = 0.033$ s^{-1} (Yang et al., 2020). C, D – stretching of thermoplastic elastomers SIS(Ba) (C) and SIS(Na) (D) with strain rate $\dot{\epsilon} = 0.01$ s^{-1} (Kajita et al., 2022).

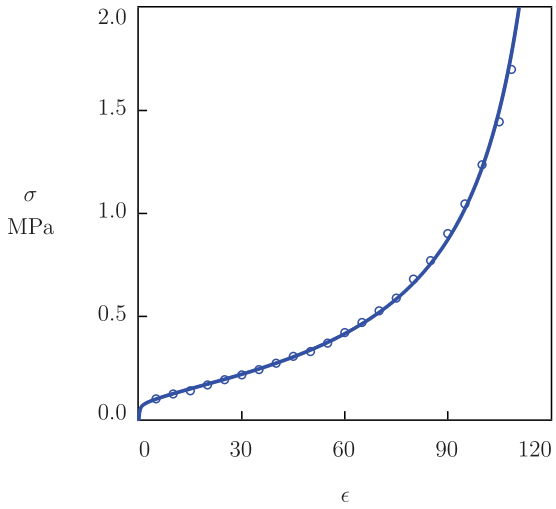

Fig. 12. Tensile stress σ versus tensile strain ϵ. Circles: experimental data (Liu et al., 2017) on poly(acrylamide) gel with CB[8]-mediated host-guest supramolecular bonds in tensile test with strain rate $\dot{\epsilon} = 0.167$ s^{-1} at room temperature. Solid line: results of numerical analysis.

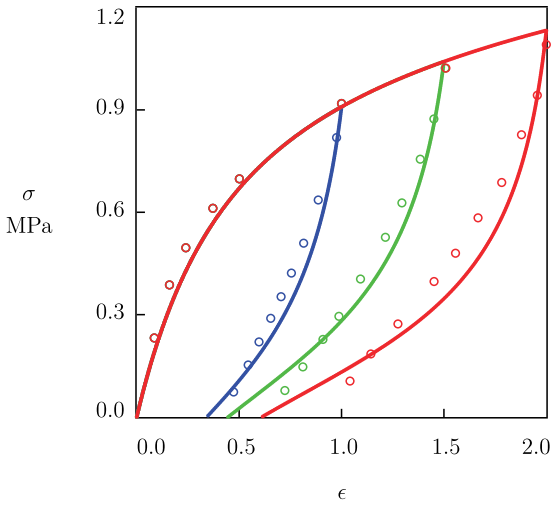

Fig. 13. Tensile stress σ versus tensile strain ϵ. Circles: experimental data (Li et al., 2021a) on PDMS-HEDS-UPy elastomer in cyclic tensile tests with strain rate $\dot{\epsilon} = 0.0167$ s^{-1} and maximum strains $\epsilon_{max} = 1.0$ (blue), 1.5 (green) and 2.0 (red). Solid lines: predictions of the model.

maximum strains $\epsilon_{max} = 0.5$ and 3.0 are depicted in Fig. 1B together with results of numerical analysis with the material coefficients listed in Tab. S2. Tab. S-2 shows that all coefficients (except for the rate of plastic flow P) are independent of maximum strain, while P decreases strongly with ϵ_{max}. Following (Drozdov and deClaville Christiansen, 2018b,c), we adopt the exponential dependence of P on ϵ_{max},

$$\log P = P_0 - P_1 \epsilon_{max},$$

determine the coefficients P_0 and P_1 with the help of the data collected in Tab. S-2, and calculate P for an arbitrary ϵ_{max}. For each maximum strain under consideration, the entire set of material parameters is reported in Tab. S-9. The stress–strain diagrams found by integration of the governing equations with these parameters are presented in Fig. 13 together with the experimental data reported by (Li et al., 2021a). This figure reveals a reasonable agreement between the data and their predictions by the model.

Figs. 1, 3, 6 and 7 show that the mechanical behavior of supramolecular elastomers can be tuned by an appropriate choice of reversible bonds. We focus on modulation of the viscoplastic response of elastomers with metal–ligand coordination bonds by changing the molar ratio n of ligands to divalent (Figs. 3 and 4) and trivalent (Figs. 6 and 9) ions. Results of numerical analysis (Figs. 6C and Fig. 9C) show that the shear modulus G, the rate of viscoplastic flow a and the

coefficient K (accounting for stress-hardening of elastomers) change consistently with the number of supramolecular linkages (the reciprocal of n). Correlations between the ligand–metal molar ratio n and the material parameters are described by Eqs. (49) and (51).

5. Conclusions

A simple model is derived for the viscoplastic behavior of supramolecular elastomers at finite strains. We focus on isothermal loading of elastomers with weak viscoelastic response at room temperature.

An advantage of the model is that describes experimental data in uniaxial tensile and compressive tests (up to breakage of specimens) and cyclic (loading–unloading) tests with the help of only four to five material constants with transparent physical meaning: (i) the shear modulus G, (ii) the coefficient K accounting for finite extensibility of chains, (iii) the rate of slippage of junctions between chains with respect to their initial positions a, (iv) the rate of plastic flow driven by inter-chain interactions P, and (v) the coefficient α characterizing slowing down of plastic deformation at retraction. The aim of this work is to evaluate how external conditions (strain rate) and micro-structure of supramolecular elastomers (type and concentration of reversible bonds) affect these quantities.

To examine the ability of the model to describe experimental stress–strain diagrams, it is applied to the analysis of observations on conventional vulcanized rubbers (Figs. 10A and 10C) and supramolecular elastomers with various types of reversible bonds (Figs. 1 to 9 and 13). Good agreement is demonstrated between the observations and results of simulation. It is shown that the material parameters change consistently with the strain rate $\dot{\epsilon}$ and composition of the elastomers.

Figs. 1 to 4 show that the classical neo-Hookean expression for the strain energy density can be used to fit the stress–strain diagrams on supramolecular elastomers under stretching with strains up to 25, provided that the viscoplastic deformation is taken into account.

Figs. 6, 7 and 9 reveal that the mechanical response of supramolecular elastomers can be modulated in a rather wide interval by an appropriate choice of reversible bonds. Eqs. (49) and (51) are proposed to predict the effect of composition on material parameters of elastomers with metal–ligand coordination bonds. The obtained results may be helpful for the design of supramolecular elastomers with required mechanical properties for stretchable and wearable electronics.

Declaration of competing interest

The authors declare that they have no known competing financial interests or personal relationships that could have appeared to influence the work reported in this paper.

Data availability

Data will be made available on request.

Acknowledgment

Financial support by Innovationsfonden (Innovation Fund Denmark, project 9091-00010B) is gratefully acknowledged.

Appendix A. Supplementary Information

Supplementary material related to this article can be found online at https://doi.org/10.1016/j.ijsolstr.2022.111919.

References

Aida, T., Meijer, E.W., Stupp, S.I., 2012. Functional supramolecular polymers. Science 335, 813–817.
Chagnon, G., Rebouah, M., Favier, D., 2015. Hyperelastic energy densities for soft biological tissues: A review. J. Elasticity 120, 129–160.
Chen, H., Hart, L.R., Hayes, W., Siviour, C.R., 2021. Mechanical characterisation and modelling of a thermoreversible superamolecular polyurethane over a wide range of rates. Polymer 221, 123607.
Drozdov, A.D., deClaville Christiansen, J., 2018a. Mechanical response of double-network gels with dynamic bonds under multi-cycle deformation. Polymer 150, 95–108.
Drozdov, A.D., deClaville Christiansen, J., 2018b. Nanocomposite gels with permanent and transient junctions under cyclic loading. Macromolecules 51, 1462–1473.
Drozdov, A.D., deClaville Christiansen, J., 2018c. Multi-cycle deformation of supramolecular elastomers: Constitutive modeling and structure–property relations. Int. J. Eng. Sci. 133, 311–335.
Drozdov, A.D., deClaville Christiansen, J., 2020a. Thermo-mechanical behavior of elastomers with dynamic covalent bonds. Int. J. Eng. Sci. 147, 103200.
Drozdov, A.D., deClaville Christiansen, J., 2020b. Self-recovery, fatigue and anti-fatigue of supramolecular elastomers. Int. J. Fatigue 134, 105496.
Drozdov, A.D., deClaville Christiansen, J., 2020c. Tension–compression asymmetry in the mechanical response of hydrogels. J. Mech. Behav. Biomed. Mater. 110, 103851.
Drozdov, A.D., deClaville Christiansen, J., 2022. Tuning the viscoelastic response of hydrogel scaffolds with covalent and dynamic bonds. J. Mech. Behav. Biomed. Mater. 130, 105179.
Drozdov, A.D., Klitkou, R., Christiansen, J.deC., 2013. Cyclic viscoplasticity of semicrystalline polymers with finite deformations. Mech. Mater. 56, 53–64.
Elziere, P., Fourton, P., Demassieux, Q., Chenneviere, A., Dalle-Ferrier, C., Creton, C., Ciccotti, M., Etienne Barthel, E., 2019. Supramolecular structure for large strain dissipation and outstanding impact resistance in polyvinylbutyral. Macromolecules 52, 7821–7830.
Fan, J., Huang, J., Gong, Z., Cao, L., Chen, Y., 2021. Toward robust, tough, self-healable supramolecular elastomers for potential application in flexible substrates. ACS Appl. Mater. Interfaces 13, 1135–1144.
Federico, S., Grillo, A., Giaquinta, G., Herzo, W., 2008. Convex fung-type potentials for biological tissues. Meccanica 43, 279–288.
Filippidi, E., Cristiani, T.R., Eisenbach, C.D., Waite, J.H., Israelachvili, J.N., Ahn, B.K., Valentine, M.T., 2017. Toughening elastomers using mussel-inspired iron-catechol complexes. Science 358, 502–505.
Gent, A.N., 1996. A new constitutive relation for rubber. Rubber Chem. Technol. 69, 59–61.
Guo, J., Long, R., Mayumi, K., Hui, C.Y., 2016. Mechanics of a dual cross-link gel with dynamic bonds: Steady state kinetics and large deformation effects. Macromolecules 49, 3497–3507.
Horgan, C.O., Saccomandi, G., 2006. Phenomenological hyperelastic strain–stiffening constitutive models for rubber. Rubber Chem. Technol. 79, 152–169.
Huo, Y., He, Z., Wang, C., Zhang, L., Xuan, Q., Wei, S., Wang, Y., Pan, D., Dong, B., Wei, R., Naik, N., Guo, Z., 2021. The recent progress of synergistic supramolecular polymers: preparation, properties and applications. Chem. Commun. 57, 1413–1429.
Imbernon, L., Norvez, S., 2016. From landfilling to vitrimer chemistry in rubber life cycle. Eur. Polym. J. 82, 347–376.
Kajita, T., Noro, A., Matsushita, Y., 2017. Design and properties of supramolecular elastomers. Polymer 128, 297–310.
Kajita, T., Noro, A., Oda, R., Hashimoto, S., 2022. Highly impact-resistant block polymer-based thermoplastic elastomers with an ionically functionalized rubber phase. ACS Omega 7, 2821–2830.
Kang, J., Tok, J.B.-H., Bao, Z., 2019. Self-healing soft electronics. Nat. Electron. 2, 144–150.
Li, J., Niu, H., Yu, Y., Gao, Y., Wu, Q., Wang, F., Sun, P., 2021a. Supramolecular polydimethylsiloxane elastomer with enhanced mechanical properties and self-healing ability engineered by synergetic dynamic bonds. ACS Appl. Polym. Mater. 3, 3373–3382.
Li, Z., Zhu, Y.-L., Niu, W., Yang, X., Jiang, Z., Lu, Z.-Y., Liu, X., Sun, J., 2021b. Healable and recyclable elastomers with record-high mechanical robustness, unprecedented crack tolerance, and superhigh elastic restorability. Adv. Mater. 33, 2101498.
Lin, J., Zheng, S.Y., Xiao, R., Yin, J., Wu, Z.L., Zheng, Q., Qian, J., 2020. Constitutive behaviors of tough physical hydrogels with dynamic metal-coordinated bonds. J. Mech. Phys. Solids 139, 103935.
Liu, K., Cheng, L., Zhang, N., Pan, H., Fan, X., Li, G., Zhang, Z., Zhao, D., Zhao, J., Yang, X., Wang, Y., Bai, R., Liu, Y., Liu, Z., Wang, S., Gong, X., Bao, Z., Gu, G., Yu, W., Yan, X., 2021. Biomimetic impact protective supramolecular polymeric materials enabled by quadruple H-bonding. J. Am. Chem. Soc. 143, 1162–1170.
Liu, J., Tan, C.S.Y., Yu, Z., Li, N., Abell, C., Scherman, O.A., 2017. Tough supramolecular polymer networks with extreme stretchability and fast room-temperature self-healing. Adv. Mater 29, 1605325.

Long, R., Mayumi, K.C., Creton, T., Narita, C.Y., 2014. Time dependent behavior of a dual cross-link self-healing gel: Theory and experiments. Macromolecules 47, 7243–7250.

Luo, J., Demchuk, Z., Zhao, X., Saito, T., Tian, M., Sokolov, A.P., Cao, P.-F., 2022. Elastic vitrimers: Beyond thermoplastic and thermoset elastomers. Matter 5, 1391–1422.

Mao, Y., Lin, S., Zhao, X., Anand, L., 2017. A large deformation viscoelastic model for double-network hydrogels. J. Mech. Phys. Solids 100, 103–130.

Martins, P.A.L.S., Natal Jorge, R.M., Ferreira, A.J.M., 2006. A comparative study of several material models for prediction of hyperelastic properties: Application to silicone-rubber and soft tissues. Strain 42, 135–147.

Mihai, L.A., Budday, S., Holzapfel, G.A., Kuhl, E., Goriely, A., 2017. A family of hyperelastic models for human brain tissue. J. Mech. Phys. Solids 106, 60–79.

Morovati, V., Dargazany, R., 2019. Micro-mechanical modeling of the stress softening in double-network hydrogels. Int. J. Solids Struct. 164, 1–11.

O'Donnell, A.D., Salimi, S., Hart, L.R., Babra, T.S., Greenland, B.W., Hayes, W., 2022. Applications of supramolecular polymer networks. React. Funct. Polym. 172, 105209.

Plagge, J., Kluppel, M., 2019. Mullins effect revisited: Relaxation, recovery and high-strain damage. Mater. Today Commun. 20, 100588.

Ray, T.R., Choi, J., Bandodkar, A.J., Krishnan, S., Gutruf, P., Tian, L., Ghaffari, R., Rogers, J.A., 2019. Bio-integrated wearable systems: A comprehensive review. Chem. Rev. 119, 5461–5533.

Richardson, B.M., Wilcox, D.G., Randolph, M.A., Anseth, K.S., 2019. Hydrazone covalent adaptable networks modulate extracellular matrix deposition for cartilage tissue engineering. Acta Biomater. 83, 71–82.

Rizwan, M., Baker, A.E.G., Shoichet, M.S., 2021. Designing hydrogels for 3D cell culture using dynamic covalent crosslinking. Adv. Healthcare Mater. 10, 2100234.

Rodin, M., Li, J., Kuckling, D., 2021. Dually cross-linked single networks: structures and applications. Chem. Soc. Rev. 50, 8147–8177.

Rosales, A.M., Anseth, K.S., 2016. The design of reversible hydrogels to capture extracellular matrix dynamics. Nat. Rev. Mater. 1 (15012).

Saadedine, M., Zairi, F., Ouali, N., Tamoud, A., Mesbah, A., 2021. A micromechanics-based model for visco-super-elastic hydrogel-based nanocomposites. Int. J. Plast. 144, 103042.

Samanta, S., Kim, S., Saito, T., Sokolov, A.P., 2021. Polymers with dynamic bonds: Adaptive functional materials for a sustainable future. J. Phys. Chem. B 125, 9389–9401.

Vernerey, F.J., 2018. Transient response of nonlinear polymer networks: A kinetic theory. J. Mech. Phys. Solids 115, 230–247.

Vernerey, F.J., Long, R., Brighenti, R., 2017. A statistically-based continuum theory for polymers with transient networks. J. Mech. Phys. Solids 107, 1–20.

Wang, S., Urban, M.W., 2020. Self-healing polymers. Nat. Rev. Mater. 5, 562–583.

Wemyss, A.M., Bowen, C., Plesse, C., Vancaeyzeele, C., Nguyen, G.T.M., Vidal, F., Wan, C., 2020. Dynamic crosslinked rubbers for a green future: A material perspective. Mater. Sci. Eng. R 141, 100561.

Wu, J., Niu, W., Zhang, S., Wu, S., Ma, W., Tang, B., 2019b. Polyacrylic acid–based coordination supramolecular elastomer with high strength, excellent fatigue-resistance, and self-recovery properties. Macromol. Chem. Phys. 220, 1800571, 2019.

Wu, X., Wang, J., Huang, J., Yang, S., 2019a. Robust, stretchable, and self-healable supramolecular elastomers synergistically cross-linked by hydrogen bonds and coordination bonds. ACS Appl. Mater. Interfaces 11, 7387–7396.

Xiang, Y., Zhong, D., Wang, P., Yin, T., Zhou, H., Yu, H., Baliga, C., Qu, S., Yang, W., 2019. A physically based visco-hyperelastic constitutive model for soft materials. J. Mech. Phys. Solids 128, 208–218.

Xu, J., Chen, W., Wang, C., Zheng, M., Ding, C., Jiang, W., Tan, L., Fu, J., 2018. Extremely stretchable, self-healable elastomers with tunable mechanical properties: Synthesis and applications. Chem. Mater. 30, 6026–6039.

Yan, X., Jin, H., Fahs, G.B., Chuang, S., Moore, R.B., Jia, L., 2017. Supramolecular elastomers. Particulate β-sheet nanocrystal–reinforced synthetic elastic networks. Polymer 121, 97–105.

Yang, Y., Du, F.-S., Li, Z.-C., 2020. Highly stretchable, self-healable, and adhesive polyurethane elastomers based on boronic ester bonds. ACS Appl. Polym. Mater. 2, 5630–5640.

Yang, B., Wei, Z., Chen, X., Wei, K., Bian, L., 2019. Manipulating the mechanical properties of biomimetic hydrogels with multivalent host-guest interactions. J. Mater. Chem. B 7, 1726–1733.

Yang, X., Yuan, D., Hou, J., Sedgwick, A.C., Xu, S., James, T.D., Wang, L., 2021. Organic/inorganic supramolecular nano-systems based on host/guest interactions. Coord. Chem. Rev. 428, 213609.

Yu, K., Xin, A., Wang, Q., 2018. Mechanics of self-healing polymer networks crosslinked by dynamic bonds. J. Mech. Phys. Solids 121, 409–431.

Zhou, J., Jiang, L., Khayat, R.E., 2018. A micro-macro constitutive model for finite-deformation viscoelasticity of elastomers with nonlinear viscosity. J. Mech. Phys. Solids 110, 137–154.